NANO LETTERS
Cite This: Nano Lett. 2019, 19, 1955−1962
Letter
pubs.acs.org/NanoLett

Thermoelectric Performance of 2D Tellurium with Accumulation Contacts

Gang Qiu,[†,‡] Shouyuan Huang,[‡,§] Mauricio Segovia,[‡,§] Prabhu K. Venuthurumilli,[‡,§] Yixiu Wang,[∥] Wenzhuo Wu,[∥] Xianfan Xu,*[,†,‡,§] and Peide D. Ye*[,†,‡]

[†]School of Electrical and Computer Engineering, Purdue University, West Lafayette, Indiana 47907, United States
[‡]Birck Nanotechnology Center, Purdue University, West Lafayette, Indiana 47907, United States
[§]School of Mechanical Engineering, Purdue University, West Lafayette, Indiana 47907, United States
[∥]School of Industrial Engineering, Purdue University, West Lafayette, Indiana 47907, United States

Supporting Information

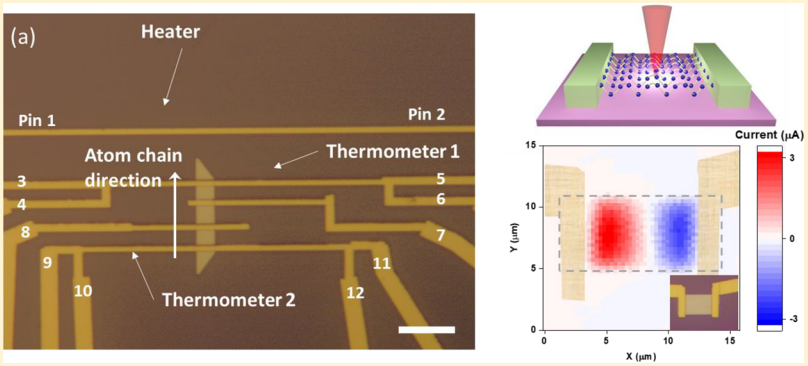

ABSTRACT: Tellurium (Te) is an intrinsically p-type-doped narrow-band gap semiconductor with an excellent electrical conductivity and low thermal conductivity. Bulk trigonal Te has been theoretically predicted and experimentally demonstrated to be an outstanding thermoelectric material with a high value of thermoelectric figure-of-merit ZT. In view of the recent progress in developing the synthesis route of 2D tellurium thin films as well as the growing trend of exploiting nanostructures as thermoelectric devices, here for the first time, we report the excellent thermoelectric performance of tellurium nanofilms, with a room-temperature power factor of 31.7 μW/cm K^2 and ZT value of 0.63. To further enhance the efficiency of harvesting thermoelectric power in nanofilm devices, thermoelectrical current mapping was performed with a laser as a heating source, and we found that high work function metals such as palladium can form rare accumulation-type metal-to-semiconductor contacts to Te, which allows thermoelectrically generated carriers to be collected more efficiently. High-performance thermoelectric Te devices have broad applications as energy harvesting devices or nanoscale Peltier coolers in microsystems.

KEYWORDS: *Tellurium, 2D Te nanofilms, metal contacts, thermoelectric, ZT*

Thermoelectricity emerges as one of the most promising solutions to the energy crisis we are facing in 21st century. It generates electricity by harvesting thermal energy from ambient or wasted heat, which is a sustainable and environment-friendly route compared to consuming fossil fuels.[1,2] The efficiency of converting heat to electricity is evaluated by the key thermoelectrical figure of merit: $ZT = S^2\frac{\sigma}{\kappa}T$, where S is the Seebeck coefficient defined as $S = \frac{\Delta V}{\Delta T}$, σ and κ are electrical and thermal conductivities, and T is the operating temperature. However, the ZT value has not been significantly enhanced since 1960s,[3] and so far the most state-of-the-art bulk materials can merely surpass 1 at room temperature.[4,5] This is because the parameters in defining ZT, Seebeck coefficient, electrical conductivity, and thermal conductivity are usually correlated through the Wiedemann−Franz law[6−8] and by engineering one parameter and generally other parameters will compensate the change, which poses a dilemma for drastically improving ZT.

For the past decades, enormous efforts have been made to increase thermoelectric efficiency along two major pathways: either by developing new high-efficiency thermoelectric bulk materials or by developing novel nanostructured thermoelectric materials.[9] From a material perspective, the paradigm of an excellent thermoelectric material should be a heavily doped narrow-band gap semiconductor with a good conductivity; meanwhile, because of the existence of a finite band gap, the separation of electrons and holes can avoid opposite

Received: December 25, 2018
Revised: February 4, 2019
Published: February 12, 2019

DOI: 10.1021/acs.nanolett.8b05144
Nano Lett. 2019, 19, 1955−1962

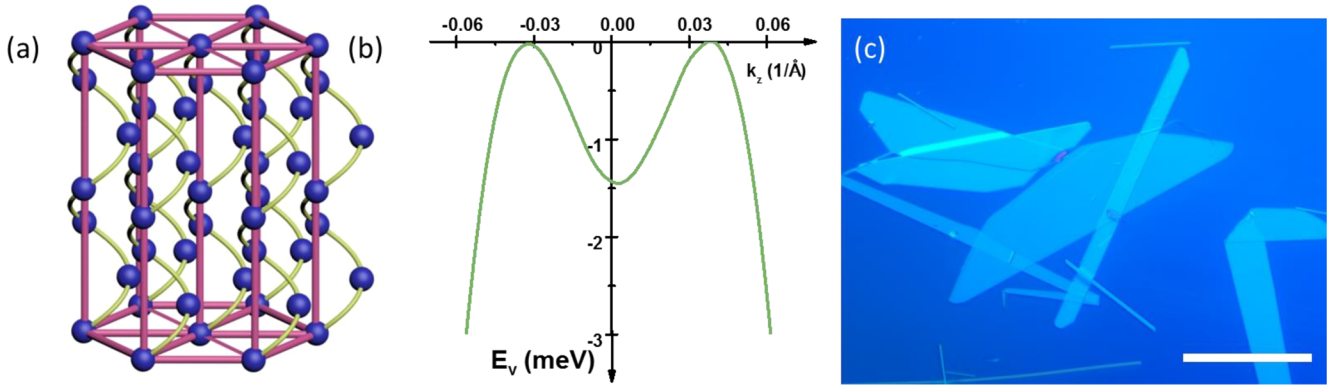

Figure 1. Atomic structure, band structure, and 2D Te nanofilms. (a) One-dimensional van der Waals (vdW) chiral structure of Te crystal. The nearest neighboring chiral chains are bonded by vdW forces into a hexagonal structure. (b) The band structure in the vicinity of valence band maxima at H point. (c) Optical image of as-grown 2D Te films dispensed onto a silicon wafer. The scale bar is 50 μm. The 1D helical chains are aligned with the long edge of Te flakes.

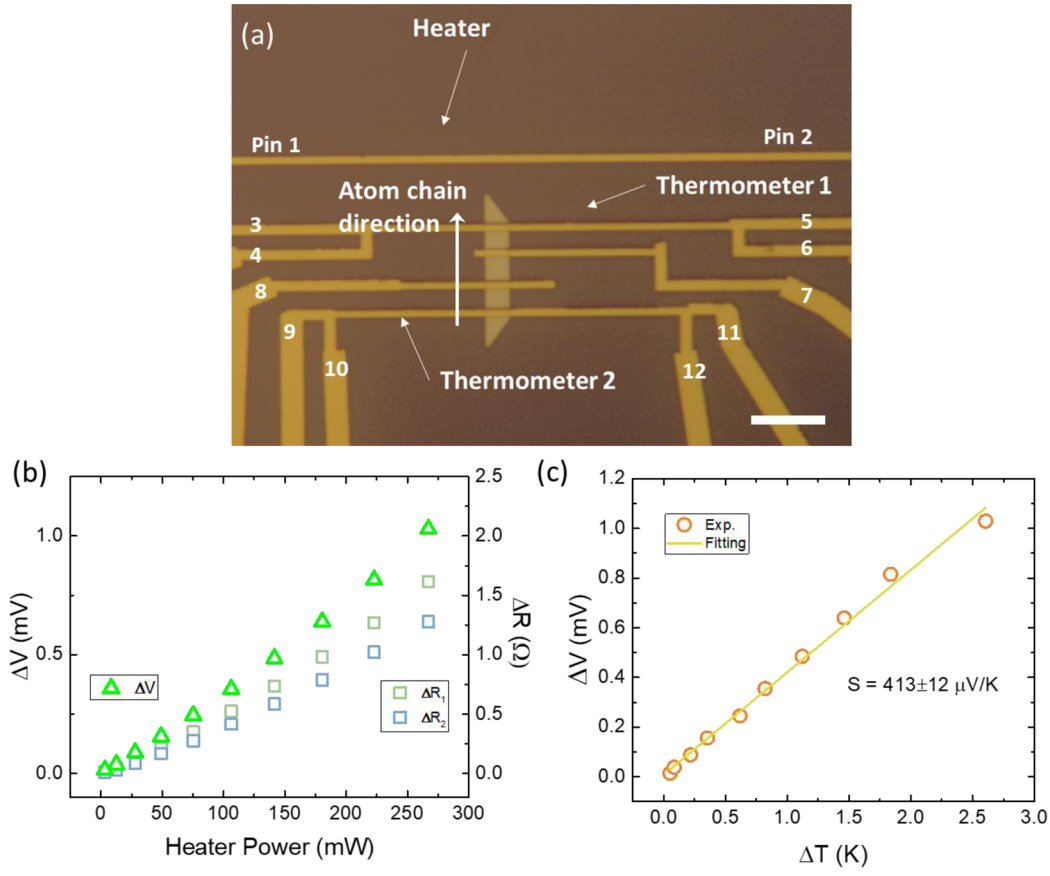

Figure 2. Seebeck coefficient measurement of 2D Te. (a) Device structure and pin-out diagram. The scale bar is 10 μm. Pins 1 and 2 are connected to the microheater that generates a temperature gradient. Pins 3–6 and Pins 9–12 are two thermometers that measure the local temperature. When combining Pins 3, 7, 8, and 9, we can also measure the conductivity of the Te film with a four-terminal configuration. (b) The voltage drop across the film and the resistance change of two thermometers as functions of heater output power. (c) The extraction of the Seebeck coefficient. The voltage drop and the temperature gradient shows a linear relationship where the slope gives the Seebeck coefficient $S = 413 \pm \mu$V/K.

contributions to the Seebeck coefficient. Also, heavy elements are preferred for thermoelectrical applications, which can enhance the ZT value by providing more effective phonon scattering centers and reducing the thermal conductivity.[1,10] Furthermore, valley engineering is also proposed recently,[11] where a higher valley degeneracy can provide multiple carrier conducting channels without affecting the Seebeck coefficient and thermal conductivity.

A structurally engineered low-dimensional nanostructure is another emerging field for thermoelectric research. The difference of mean free path between electrons and phonons provides us with a chance to disentangle the correlation between the electrical conductivity and thermal conductivity governed by the Wiedemann–Franz law. Therefore, low-dimensional nanostructures in certain material systems may impede the acoustic phonon propagating, whereas electrons

DOI: 10.1021/acs.nanolett.8b05144
Nano Lett. 2019, 19, 1955–1962

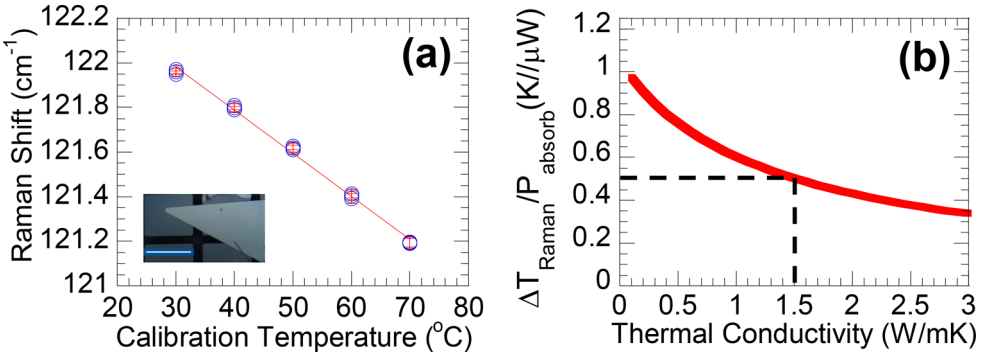

Figure 3. Measurement of in-plane thermal conductivity using micro-Raman thermometry. (a) Calibrated Raman spectrum (A1 mode) vs temperature as the micro-thermometry. Inset: optical image of the Te thin film, scale bar 30 μm. (b) Numerical modeling result of temperature rise per absorbed laser power. Dashed lines indicate the in-plane thermal conductivity of 1.50 W/m K, corresponding to the measurement temperature rise per absorbed laser power of 0.503 K/μW.

can be transmitted less interrupted. Therefore, the thermal conductivity of the nanostructure material system is suppressed without significantly degrading electrical conductivity.[2,9,12] Moreover, when the characteristic length of the nanostructure geometry is small enough to influence the band structure because of the quantum confinement effect, the profile of density of states (DOS) can evolve into sharp shapes at band edges, which boosts the Seebeck coefficient, since the Seebeck coefficient is related with how fast DOS changes near the Fermi energy.[9,13]

Trigonal tellurium is a simple but ideal material system for thermoelectric application, which meets almost all of the aforementioned criteria of a good thermoelectric material. Bulk Te has been theoretically predicted[14] and experimentally demonstrated[15] with a high thermoelectric performance because it is a heavily doped narrow-band gap semiconductor with a good electrical conductivity. On the other hand, Te is the heaviest stable (i.e., nonradioactive) nonmetallic element (excluding noble gases); therefore, it has a very low thermal conductivity due to the heavy atom mass, which also contributes to a higher thermoelectrical efficiency. Recently, with a more comprehensive band structure of Te being revealed,[16,17] it has been revisited for a new generation of thermoelectric materials[18−20] due to its strong spin−orbit coupling, which leads to a band splitting and quadruple band degeneracy near the edge of the valence band.[21]

Here, utilizing the intrinsic high thermoelectric performance of tellurium (Te) combined with the advantage of nanostructures, we report highly efficient thermoelectric devices fabricated from two-dimensional Te nanofilms. A recently proposed and demonstrated liquid phase synthesis approach allows us to acquire large-scale ultrathin 2D Te nanofilms with a high crystal quality,[22,23] which enables the exploration of its application for electronics,[22,24,25] piezo-electronics,[26] and optoelectronics.[27] In this Letter, we focus on investigating the thermoelectric performance of tellurium nanofilm devices.

Results. Figure 1a shows the atomic structure of the trigonal Te lattices. Covalently bonded atomic helical chains stretching in one direction are packed in parallel into hexagonal lattices. Each atomic chain is weakly bonded to six nearest neighboring chains; therefore, tellurium can be considered as a one-dimensional (1D) material, as an analogy to two-dimensional (2D) materials such as graphene, molybdenum disulfide (MoS_2), and black phosphorus. Bulk Te has a narrow direct band gap (~0.35 eV) at H point of the Brillouin zone, with a camel back feature at the vicinity of valence band maxima[14,22] (see Figure 1b). With a recently proposed and demonstrated solution-based hydrothermal process,[22,23] large-area high-quality 2D Te films can be grown with a thickness ranging from monolayer to tens of nanometers. Figure 1c shows typical as-grown Te nanofilms dispensed onto a Si wafer with a 300 nm SiO_2 capping layer, with spiral atomic chains laying in parallel along the longer edge of the films (shown in Figure 2a), as confirmed by TEM[22] and the angle-resolved Raman spectroscopy method.[23] The crystal orientation suggests these Te films, despite its 1D nature, resemble 2D van der Waals materials such as graphene with a dangling bond-free interface, which allows us to explore the thermoelectric performance of 2D Te films.

To measure the Seebeck coefficient and conductivity of 2D Te, a thermoelectric measurement device was designed and fabricated, as shown in Figure 2a with a 31 nm thick device in an optical image, similar to the measurement setup for other low-dimensional materials such as carbon nanotubes,[28,29] graphene,[30−32] MoS_2,[33] and SnS_2.[34] Two four-terminal micro-thermometers (Pins 3−6 and Pins 9−12) were placed at two ends of a Te flake along the atom chain direction (as denoted in Figure 2a) to measure the local temperature as well as the voltage drop simultaneously. The thermometer filaments were made of a 100 nm thick platinum (Pt) nanostrip because Pt shows a good linearity of the temperature coefficient for a broad temperature region including room temperature. The temperature versus resistance curve was calibrated and plotted in Figure S1. Ten nm nickel was deposited underneath Pt for better adhesion. A microheater (Pin 1 and Pin 2) was placed near one side of the flake to generate a temperature gradient. The microheater was designed intentionally at least one order longer (>200 μm) than the spacing and the flake size so that 1D thermal transport approximation is applicable. Two additional contacts (Pin 7 and Pin 8) were placed on Te as probes to measure the electrical conductivity of Te with a standard four-terminal configuration. By applying a certain voltage onto the microheater (between Pin 1 and Pin 2), the heating power was added to the system. The voltage drop was measured across the flake between Pin 3 and Pin 9 after a sufficiently long time until the system reaches equilibrium and the voltage was settled. The resistance of the thermometer was also measured with a four-terminal configuration and was converted into a local temperature using the calibrated temperature vs resistance curve (Figure S1). We observed a

DOI: 10.1021/acs.nanolett.8b05144
Nano Lett. 2019, 19, 1955−1962

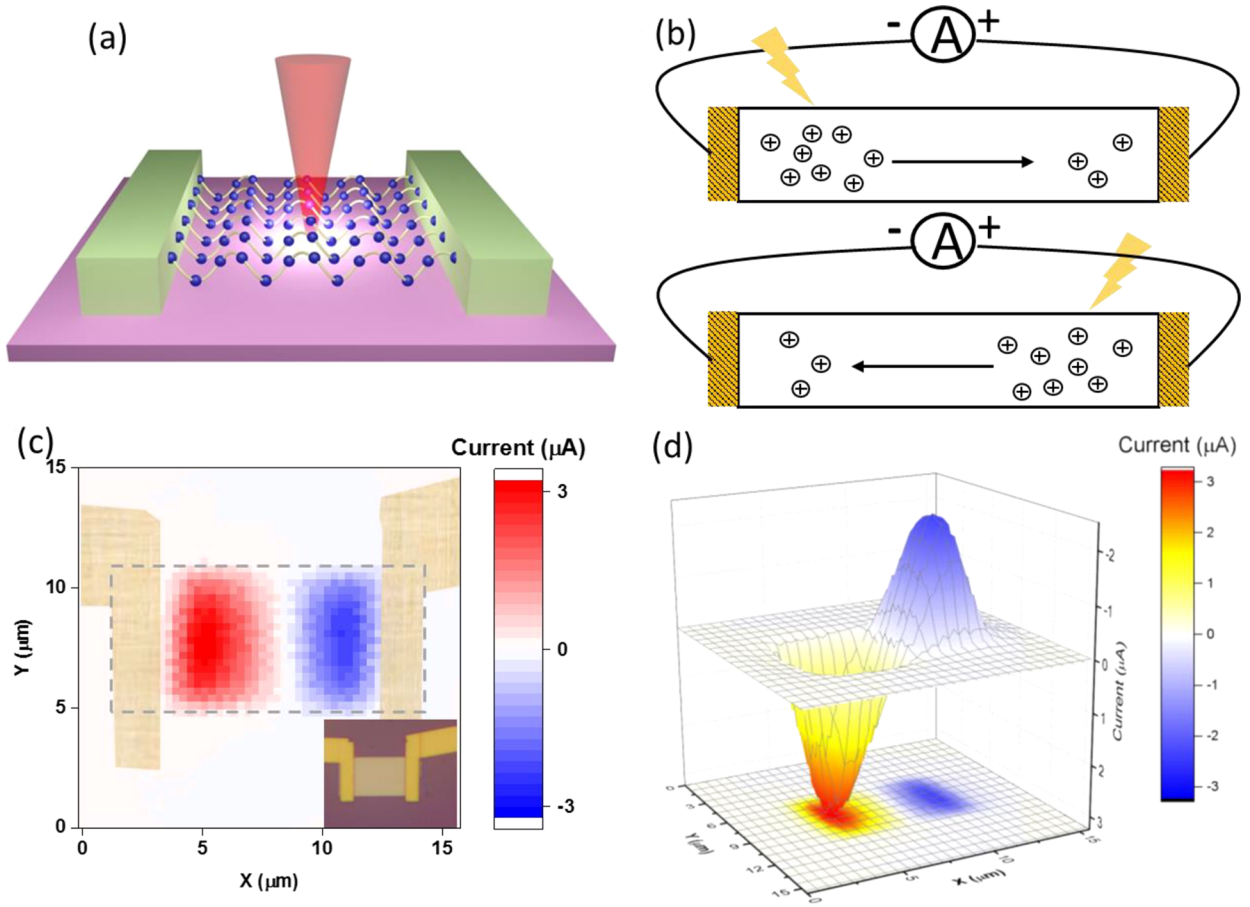

Figure 4. Laser-induced thermoelectric (LITE) current mapping. (a) Schematics of the experiment setup. Two Ni contacts were patterned onto the flake. A 633 nm He−Ne laser was used to heat up the flake locally. (b) The principle of LITE mapping. For p-type devices, when the laser illuminates the left side of the flake (top panel), the carrier concentration of the left will be higher than the right side, which induces a diffusion current from the left to right inside the flake. When the laser shines on the right side, the current direction will be flipped (bottom panel). (c) The LIFE current mapping of the real device. The inset is the optical image of the same device. (d) The LITE current mapping in a 3D plot.

monotonic increase in the voltage drop and temperature gradient as we raised the output power (Figure 2b), and the temperature rise on thermometer 1 was slightly higher compared to thermometer 2 since it is closer to the heating source. The voltage drop ΔV is plotted against the temperature difference across the flake ΔT (see Figure 2c) with a linear trend, from whose slope we can extract the Seebeck coefficient to be $S = \Delta V/\Delta T = 413\ \mu$V/K. Furthermore, the conductivity of Te films can also be measured with a four-terminal configuration using Pins 1, 7, 8, and 9. The measured Seebeck coefficient and conductivity gives a high value of power factor, which takes the form: PF = $S^2\sigma$ = 31.7 μW/cm K^2. The thermal conductivity along the 1D chain direction of a 35 nm thick Te film is measured using the micro-Raman spectroscopy technique[35] on the suspended 2D Te film (Figure 3). The micro-Raman method uses the calibrated temperature-dependent Raman shift as a micro-thermometer (Figure 3a). The laser focal line heats up the suspended tellurium film and measures temperature using the induced Raman scattering at the same time. Compared to the numerical model (Figure 3b), the thermal conductivity is extracted to be about 1.50 W/m K. (Also see the Method section and Supporting Information, Note 5, for the measurement details.) This thermal conductivity value is lower than that of bulk Te around 3 W/m K,[36] which is reasonable considering phonon scattering at the surfaces reduces thermal conductivity of thin films. On the basis of the measured thermal conductivity of Te films, we can derive a room-temperature ZT value of 0.63, a significant boost from the ZT value reported in bulk Te[14,15] (0.2−0.3).

To exploit the advantage of thermoelectric effect in nanostructures, we not only need an excellent thermoelectric material to convert the thermal energy into electricity but also need well-engineered devices to efficiently "collect" the electricity, especially in nanoscale devices. One of the fundamental challenges of a semiconductor device is the Schottky contact, which is usually formed on a metal−semiconductor interface with a large contact resistance and reduces the device efficiency and consumes additional power. In the next section, we will discuss how different kinds of metal contacts will affect the efficiency of harvesting thermoelectric power and use the laser-induced thermoelectrical (LITE) current mapping technique to visualize the depletion-mode, neutral-mode, and accumulation-mode contacts as well as the thermoelectric current distribution across the 2D Te devices.

The experiment setup is shown schematically in Figure 4a. A He−Ne laser with a wavelength of 633 nm was used to locally heat the flake and create a temperature gradient. The short-circuit thermoelectric current was monitored by connecting a multimeter to the two metal contacts, and by moving the sample stage, we can spatially map the LITE current. The radius of the laser beam size is ∼1 μm (see the Method section) through a confocal microscope in order to get a better

DOI: 10.1021/acs.nanolett.8b05144
Nano Lett. 2019, 19, 1955−1962

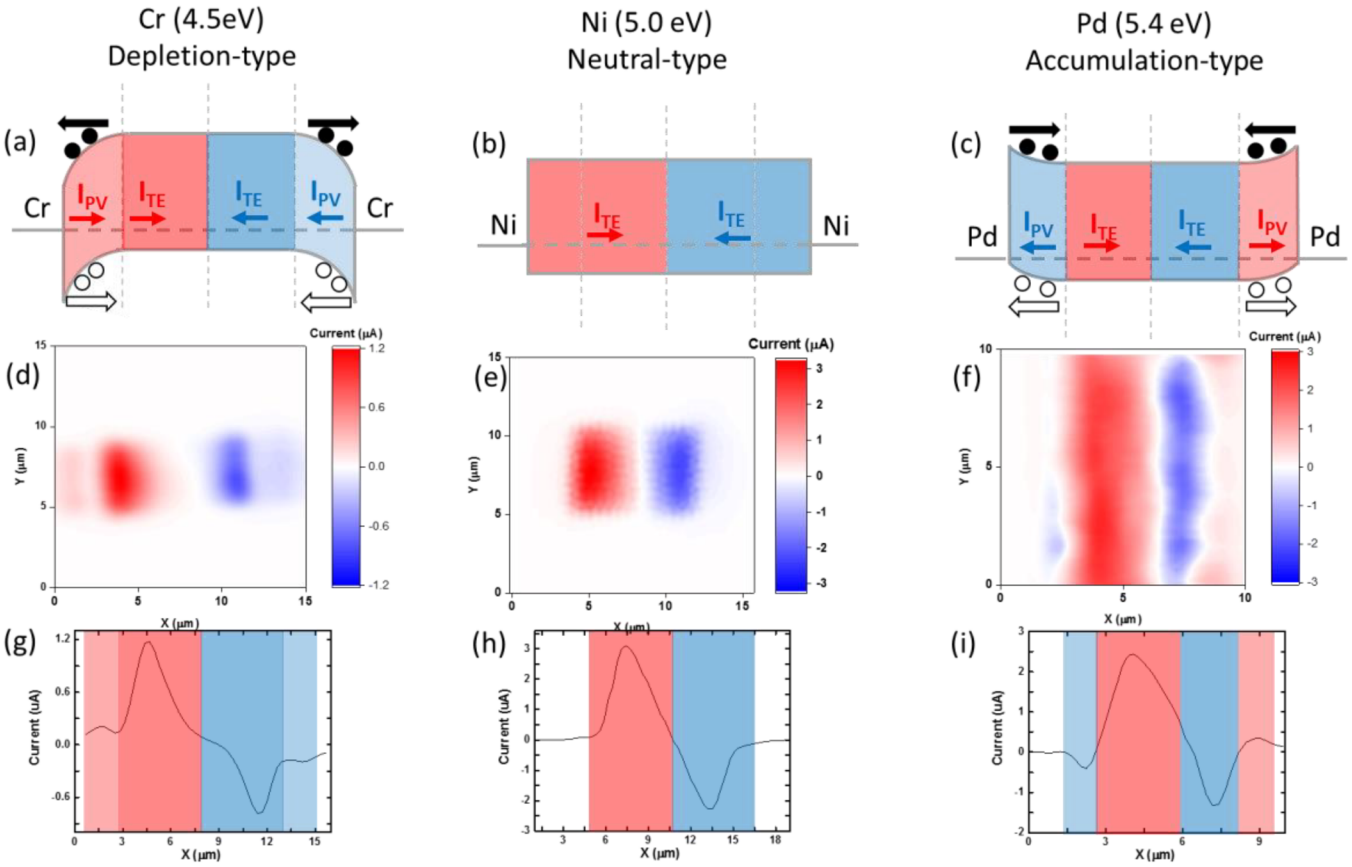

Figure 5. Visualizing three types of metal-to-semiconductor contacts by laser-induced current mapping. (a–c) Band diagrams of depletion-type (Cr-contacted), neutral-type (Ni-contacted), and accumulation-type (Pd-contacted) devices. The laser-induced current mapping will be the superposition of the thermoelectric current (I_{TE}) in the middle region and the photovoltaic current (I_{PV}) at the interface. (d–f) Current mapping of three devices with Cr, Ni, and Pd contacts. The red and blue colors correspond to the current flow to the right and to the left, respectively, the same as in parts a–c. (g–i) The line profile of the current distribution cut along the center of the channel in three devices.

spatial resolution. When the laser illuminates the left side of the flake, the local temperature of this side will be higher than the right. Therefore, the carrier concentration of the left end will also be higher, which creates a density gradient and the diffusion current flows from left to right, as described in the top panel of Figure 4b. Similarly, when the laser spot moves to the right, the thermoelectric current will flip the sign. Figure 4c shows an optical image of a typical device with Ni contacts and its corresponding LITE current mapping. The thicknesses of the films we used for LITE measurements are in the range 10–15 nm. In Figure 4c, the positive sign (red region in the plot) corresponds the current flowing from the left end of the device toward the right end, and the negative sign (blue) is the other way around, as we expected for the p-type semiconductor in Figure 4b. Also it is worth it to mention that we achieved over a 3 μA thermoelectric current under a 3 mW laser power, which is at least two orders higher (normalized with laser power) than other reported 2D thin film devices such as SnS_2[34] and MoS_2[33] with similar photothermoelectric measurements.

One concern for interpreting the LITE current mapping is that photovoltaic effect may mix into the thermoelectric effect and, therefore, contribute to the total current. Note that, in a symmetric device structure as in Figure 4c, there is no band tilting in the channel region. The photovoltaic effect only occurs when the laser spot moves to the metal-to-semiconductor interface where the misalignment between the metal work function and semiconductor Fermi level causes the formation a Schottky barrier and introduces an electrical field, which will collect the photogenerated electron and hole pairs. The electrical field at two contacts will be in the opposite direction, and the photovoltaic current mapping profile may show some resemblance to the thermoelectrical current. One needs to carefully deal with this issue and isolate these two components spatially as discussed by Lee et al. in the SnS_2 device.[34] The Schottky barrier width (the width of band-bending region), strongly related with carrier concentration, is usually less than 1 μm in heavily doped semiconductors. Hence the photovoltaic current can only be detected within the narrow region at the metal-to-semiconductor interface, whereas the thermoelectric current should be observed through the entire flake with a gradual change from a positive to negative value, as shown in Figure 4c,d. We can use this difference to spatially separate these two components.

Here we changed metals with a different work function to understand the impact of contact metals on the photovoltaic effect. There are in general three types of metal-to-semiconductor contacts:[37] accumulation-type, neutral-type (near flat-band condition), and depletion-type, depending on the alignment of the metal work function and semiconductor Fermi level, as shown in Figure 5a,d,g. In principle, by changing the metal work function, we should be able to achieve all three types of contacts on the same semiconductor. However, the contact profile is difficult to alter experimentally

DOI: 10.1021/acs.nanolett.8b05144
Nano Lett. 2019, 19, 1955–1962

in most of traditional 3D semiconductors such as Si, Ge, and III−V due to the strong Fermi-level pinning effect. For instance, in silicon, the contact is usually pinned approximately 1/3 of the band gap near the valence band to form a depletion contact no matter what metal contact is used.[35] It is believed that the dangling bonds at the semiconductor interface will introduce a high density of the midband gap interface states that should be preferentially filled when the metal encounters the semiconductor.[37−39] Therefore, it is difficult to form an accumulation contact (especially in p-type semiconductors[40]) for good ohmic contacts. It is widely believed that the Fermi-level pinning issue is less severe in 2D vdW semiconductors than in traditional bulk 3D semiconductors, thanks to their dangling bond-free crystal surface. The pinning factor in 2D materials has even been reported to approach unity, which means no Fermi-level pinning, using the transferred contact technique.[41] Here we adopted three different metals: Pd (work function Ψ_M of 5.4 eV), Ni (5.0 eV), and Cr (4.5 eV) for thermoelectric current mapping.

The results of photocurrent mapping on three devices with different metal contacts are presented in Figure 5. The Cr-contacted device shows four distinctive areas with a different current origin (see Figure 5d): the middle red and blue area is the thermally generated current and the outer zones are the photovoltaic current generated at the Schottky contacts. By comparing the optical image and the current mapping, we noticed the center of the outer zone is located exactly at the metal-to-semiconductor interface, which confirms the origin of photovoltaic current. According to the polarity of the photovoltaic current, we can deduce that the band at the semiconductor boundary is bending downward to form a depletion-type contact (shown in Figure 5a), which is the most common case.

In contrast, the Ni-contacted device only has two distinctive thermoelectric current areas (Figure 5b,e), indicating there is almost no band bending within our instrument detecting range at the contact region (Figure 5h). This corresponds to the flat-band situation, which is represented in Figure 5b. As we adopted higher work function metal Pd, we noticed that the polarity of the photovoltaic current has inverted compared to the Cr-contacted device (Figure 5f,i, indicating accumulation-type contacts are formed. This suggests Ni and Pd can form near Ohmic metal-to-semiconductor contacts with essentially no Schottky barrier, which explains why the record low contact resistance can be achieved in 2D Te transistors with Pd contacts.[22] It is worth mentioning that such accumulation-type contacts are very rare cases, especially in p-type semiconductors. The tunable contact band-bending profile can be ascribed to the depinning effect at the vdW interface. We also noticed that the thermoelectric current is 3 times larger in Pd- and Ni-contacted devices compared to the Cr-contacted device, indicating that high-quality contacts are necessary to collect thermally generated carriers and to harvest the thermoelectric energy more efficiently. By taking advantage of different metal contacts, we can also tune the behavior of Te Schottky transistors (see Figure S2), or implement device structures with versatile functionalities such as Te Schottky diodes with an on/off ratio over 10^3 at room temperature (see Figure S3) and solar cell devices (see Figure S4).

In summary, we present a newly developed hydrothermally synthesized versatile 2D Te nanofilm as a promising candidate for thermoelectric applications, given its high electrical conductivity, low thermal conductivity, and two-dimensionality. The room-temperature Seebeck coefficient, power factor, and ZT value were measured to be 413 μV/K, 31.7 μW/cm K^2, and 0.63, respectively, on a 31 nm thick 2D Te film. Laser-induced current mappings were performed to visualize the thermoelectric current distribution as well as to understand how the metal-to-semiconductor contacts will impact the efficiency of harvesting thermoelectric power. We observed and identified three distinctive contact types with three different metals. Among them, accumulation-type contacts were clearly observed in p-type 2D semiconductors for the first time. Our work finds a niche to apply 2D Te as a potential thermoelectric material for microenergy harvesting systems or as micro-Peltier coolers. Moreover, the tunable metal-to-semiconductor contacts allow us to design high-performance thermoelectrical devices and other electronics with novel functionalities.

Method. *Device Fabrication.* The 2D Te flakes were synthesized and transferred onto a silicon wafer with a 90 nm SiO_2 capping layer following the procedure reported in ref 18. The devices were patterned with electron beam lithography (EBL). Then, 10 nm Ni and 100 nm Pt were deposited with an electron beam evaporator as two thermometers since Pt has a better linearity in the temperature coefficient; 10 nm Ni and 100 nm Au were deposited for the rest of the contacts.

The devices for the current mapping experiment were fabricated with a similar procedure, except that three different types of metals were deposited (30:100 nm Cr/Au, 30:100 nm Ni/Au, 30:100 nm Pd/Au).

Seebeck Coefficient and Power Factor Measurement. A heating power was added to the system by applying a dc voltage (from 1 to 10 V) across the heater with a Keithley 2450 voltage source meter. After a sufficiently long time, the system reaches equilibrium, and the voltage drop and temperature gradient stabilized. The voltage difference across the flake was measured with a Keithley 2182A nanovoltmeter. The resistance of two thermometers were measured with a synchronized Keithley 6221 current source meter and Keithley 2182A nanovoltmeter in δ mode, and the local temperatures were determined by converting the resistance of the thermometer into temperature through the precalibrated temperature versus resistance curve. The electrical conductivity of Te films was measured in a four-terminal configuration using the SR830 lock-in amplifier with standard ac measurement techniques.

In-Plane Thermal Conductivity Measured Using the Micro-Raman Method. The thin film tellurium sample (35 nm) for the thermal conductivity measurement is suspended on a silicon trench (5 μm wide, 13 μm deep) by the PDMS stamping method[42] using the Langmuir−Blodgett transfer process.[22] A 633 nm He−Ne laser beam is diffracted through a slit and then focused using a 100× objective into a laser focal line. The length of the laser focal line is 7.5 μm and is along the direction of the silicon trench, and the width is 0.45 μm, positioned at the center of the suspending region. The laser focal line heats up the tellurium film, creating a temperature gradient and inducing Raman scattering at the same time. The Raman scattering signal is collected and sent to a spectrometer (Horiba LabRam). With the Raman peak shift with temperature calibrated, the Raman signal can be used as a thermometer. Laser absorption by the tellurium film is determined by measuring reflection and transmission. The thermal conductivity can then be extracted using a heat transfer model with the knowledge of laser absorption, Raman

DOI: 10.1021/acs.nanolett.8b05144
Nano Lett. 2019, 19, 1955−1962

shift/temperature, and geometry. This method is adapted from our previous works for measuring the in-plane thermal conductivity of 2D materials.[32,43,44]

Laser-Induced Current Mapping. The photocurrent is driven by a normal incident He−Ne laser (633 nm). The light is focused by a 50× long working-distance objective (Nikon CF Plan 50× EPI SLWD, N_A 0.45) to a w_0 = 0.96 μm spot (measured by the standard knife-edge method). A Keithley 2612a source meter is coupled with a piezoelectric nanopositioner (MadCityLab NanoLP-100) to conduct the spatial mapping of current measurement. The photocurrent is measured at zero bias, V_{ds} = 0 V.

■ ASSOCIATED CONTENT

Supporting Information

The Supporting Information is available free of charge on the ACS Publications website at DOI: 10.1021/acs.nanolett.8b05144.

Calibrating the temperature coefficient of Pt thermometers, multiple channel transistors with different metal contacts on the same flake, Te-based Schottky diode devices, demonstration of a solar cell device based on Te Schottky diodes, and measurement of in-plane thermal conductivity using micro-Raman thermometry (PDF)

■ AUTHOR INFORMATION

Corresponding Authors

*E-mail: xxu@ecn.purdue.edu.

*E-mail: yep@purdue.edu.

ORCID

Xianfan Xu: 0000-0003-0580-4625

Peide D. Ye: 0000-0001-8466-9745

Notes

The authors declare no competing financial interest.

■ REFERENCES

(1) Bhandari, C. M.; Rowe, D. M. *CRC Handbook of Thermoelectrics*; CRC Press: Boca Raton, FL, 1995.

(2) Rowe, D. M. *Thermoelectrics Handbook: Macro to Nano*; CRC/Taylor & Francis: Boca Raton, FL, 2006.

(3) Wright, D. A. Thermoelectric Properties of Bismuth Telluride and Its Alloys. *Nature* **1958**, *181*, 834−834.

(4) Polvani, D. A.; Meng, J. F.; Chandra Shekar, N. V.; Sharp, J.; Badding, J. V. Large Improvement in Thermoelectric Properties in Pressure-Tuned p-Type $Sb_{1.5}Bi_{0.5}Te_3$. *Chem. Mater.* **2001**, *13* (6), 2068−2071.

(5) Venkatasubramanian, R.; Siivola, E.; Colpitts, T.; O'Quinn, B. Thin-Film Thermoelectric Devices with High Room-Temperature Figures of Merit. *Nature* **2001**, *413* (6856), 597−602.

(6) Jones, W.; March, N. H. *Theoretical Solid State Physics: Perfect Lattices in Equilibrium*; Courier Corporation: New York, 1985.

(7) Kittel, C.; McEuen, P.; McEuen, P. *Introduction to Solid State Physics*; Wiley New York: New York, 1996.

(8) Bejan, A.; Kraus, A. D. *Heat Transfer Handbook*; John Wiley & Sons: New York, 2003; Vol. *1*.

(9) Dresselhaus, M. S.; Chen, G.; Tang, M. Y.; Yang, R.; Lee, H.; Wang, D.; Ren, Z.; Fleurial, J. P.; Gogna, P. New Directions for Low-Dimensional Thermoelectric Materials. *Adv. Mater.* **2007**, *19* (8), 1043−1053.

(10) DiSalvo, F. J. Thermoelectric Cooling and Power Generation. *Science* **1999**, *285*, 703−706.

(11) Pei, Y.; Shi, X.; Lalonde, A.; Wang, H.; Chen, L.; Snyder, G. J. Convergence of Electronic Bands for High Performance Bulk Thermoelectrics. *Nature* **2011**, *473* (7345), 66−69.

(12) Heremans, J. P.; Dresselhaus, M. S.; Bell, L. E.; Morelli, D. T. When Thermoelectrics Reached the Nanoscale. *Nat. Nanotechnol.* **2013**, *8*, 471−473.

(13) Zeng, J.; He, X.; Liang, S.-J.; Liu, E.; Sun, Y.; Pan, C.; Wang, Y.; Cao, T.; Liu, X.; Wang, X.; et al. Experimental Identification of Critical Condition for Drastically Enhancing Thermoelectric Power Factor of Two-Dimensional Layered Materials. *Nano Lett.* **2018**, *18* (12), 7538−7545.

(14) Peng, H.; Kioussis, N.; Snyder, G. J. Elemental Tellurium as a Chiral P-Type Thermoelectric Material. *Phys. Rev. B: Condens. Matter Mater. Phys.* **2014**, *89* (19), 195206.

(15) Lin, S.; Li, W.; Chen, Z.; Shen, J.; Ge, B.; Pei, Y. Tellurium as a High-Performance Elemental Thermoelectric. *Nat. Commun.* **2016**, *7*, 10287.

(16) Nakayama, K.; Kuno, M.; Yamauchi, K.; Souma, S.; Sugawara, K.; Oguchi, T.; Sato, T.; Takahashi, T. Band Splitting and Weyl Nodes in Trigonal Tellurium Studied by Angle-Resolved Photoemission Spectroscopy and Density Functional Theory. *Phys. Rev. B: Condens. Matter Mater. Phys.* **2017**, *95* (12), 125204.

(17) Agapito, L. A.; Kioussis, N.; Goddard, W. A.; Ong, N. P. Novel Family of Chiral-Based Topological Insulators: Elemental Tellurium under Strain. *Phys. Rev. Lett.* **2013**, *110* (17), 176401.

(18) Sharma, S.; Singh, N.; Schwingenschlögl, U. Two-Dimensional Tellurene as Excellent Thermoelectric Material. *ACS Appl. Energy Mater.* **2018**, *1* (5), 1950−1954.

(19) Lin, C.; Cheng, W.; Chai, G.; Zhang, H. Thermoelectric Properties of Two-Dimensional Selenene and Tellurene from Group-VI Elements. *Phys. Chem. Chem. Phys.* **2018**, *20*, 24250−24256.

(20) Gao, Z.; Tao, F.; Ren, J. Unusually Low Thermal Conductivity of Atomically Thin 2D Tellurium. *Nanoscale* **2018**, *10* (27), 12997−13003.

(21) Qiu, G.; Wang, Y.; Nie, Y.; Zheng, Y.; Cho, K.; Wu, W.; Ye, P. D. Quantum Transport and Band Structure Evolution under High Magnetic Field in Few-Layer Tellurene. *Nano Lett.* **2018**, *18*, 5760−5767.

(22) Wang, Y.; Qiu, G.; Wang, R.; Huang, S.; Wang, Q.; Liu, Y.; Du, Y.; Goddard, W. A.; Kim, M. J.; Xu, X.; et al. Field-Effect Transistors Made from Solution-Grown Two-Dimensional Tellurene. *Nat. Electron.* **2018**, *1* (4), 228−236.

(23) Du, Y.; Qiu, G.; Wang, Y.; Si, M.; Xu, X.; Wu, W.; Ye, P. D. One-Dimensional van Der Waals Material Tellurium: Raman Spectroscopy under Strain and Magneto-Transport. *Nano Lett.* **2017**, *17*, 3965−3973.

(24) Qiu, G.; Si, M.; Wang, Y.; Lyu, X.; Wu, W.; Ye, P. D. High-Performance Few-Layer Tellurium CMOS Devices Enabled by Atomic Layer Deposited Dielectric Doping Technique. *2018 76th Device Res.Conf.* **2018**, *06202* (2017), 1−2.

(25) Wu, W.; Qiu, G.; Wang, Y.; Wang, R.; Ye, P. Tellurene: Its Physical Properties, Scalable Nanomanufacturing, and Device Applications. *Chem. Soc. Rev.* **2018**, *47* (19), 7203−7212.

(26) Gao, S.; Wang, Y.; Wang, R.; Wu, W. Piezotronic Effect in 1D van Der Waals Solid of Elemental Tellurium Nanobelt for Smart Adaptive Electronics. *Semicond. Sci. Technol.* **2017**, *32* (10), 104004.

(27) Amani, M.; Tan, C.; Zhang, G.; Zhao, C.; Bullock, J.; Song, X.; Kim, H.; Shrestha, V. R.; Gao, Y.; Crozier, K. B.; et al. Solution-Synthesized High-Mobility Tellurium Nanoflakes for Short-Wave Infrared Photodetectors. *ACS Nano* **2018**, *12* (7), 7253−7263.

(28) Kim, P.; Shi, L.; Majumdar, A.; McEuen, P. L. Thermal Transport Measurements of Individual Multiwalled Nanotubes. *Phys. Rev. Lett.* **2001**, *87* (21), 215502.

(29) Shi, L.; Li, D.; Yu, C.; Jang, W.; Kim, D.; Yao, Z.; Kim, P.; Majumdar, A. Measuring Thermal and Thermoelectric Properties of One-dimensional Nanostructures Using a Microfabricated Device. *J. Heat Transfer* **2003**, *125* (5), 881−888.

(30) Seol, J. H.; Jo, I.; Moore, A. L.; Lindsay, L.; Aitken, Z. H.; Pettes, M. T.; Li, X.; Yao, Z.; Huang, R.; Broido, D.; Mingo, N.; Ruoff, R.S.; Shi, L.; et al. Two-dimensional Phonon Transport in Supported Graphene. *Science* **2010**, *328* (5975), 213−216.

DOI: 10.1021/acs.nanolett.8b05144
Nano Lett. 2019, 19, 1955−1962

(31) Gehring, P.; Harzheim, A.; Spiece, J.; Sheng, Y.; Rogers, G.; Evangeli, C.; Mishra, A.; Robinson, B. J.; Porfyrakis, K.; Warner, J. H.; et al. Field-Effect Control of Graphene-Fullerene Thermoelectric Nanodevices. *Nano Lett.* **2017**, *17*, 7055−7061.
(32) Kodama, T.; Ohnishi, M.; Park, W.; Shiga, T.; Park, J.; Shimada, T.; Shinohara, H.; Shiomi, J.; Goodson, K. E. Modulation of Thermal and Thermoelectric Transport in Individual Carbon Nanotubes by Fullerene Encapsulation. *Nat. Mater.* **2017**, *16*, 892.
(33) Kayyalha, M.; Maassen, J.; Lundstrom, M.; Shi, L.; Chen, Y. P. Gate-Tunable and Thickness-Dependent Electronic and Thermoelectric Transport in Few-Layer MoS_2. *J. Appl. Phys.* **2016**, *120* (13), 134305.
(34) Lee, M.-J.; Ahn, J.-H.; Sung, J. H.; Heo, H.; Jeon, S. G.; Lee, W.; Song, J. Y.; Hong, K.-H.; Choi, B.; Lee, S.-H.; et al. Thermoelectric Materials by Using Two-Dimensional Materials with Negative Correlation between Electrical and Thermal Conductivity. *Nat. Nat. Commun.* **2016**, *7*, 12011.
(35) Luo, Z.; Maassen, J.; Deng, Y.; Du, Y.; Lundstrom, M. S.; Ye, P. D.; Xu, X.; Garrelts, R. P. Anisotropic In-Plane Thermal Conductivity Observed in Few-Layer Black Phosphorus. *Nat. Commun.* **2015**, *6*, 8572.
(36) Ho, C. Y.; Powell, R. W.; Liley, P. E. Thermal Conductivity of the Elements. *J. Phys. Chem. Ref. Data* **1972**, *1* (2), 279−421.
(37) Sze, S. M.; Ng, K. K. *Physics of Semiconductor Devices*; John Wiley & Sons: New York, 2006.
(38) Allen, F. G.; Gobeli, G. W. Work Function, Photoelectric Threshold, and Surface States of Atomically Clean Silicon. *Phys. Rev.* **1962**, *127* (1), 150.
(39) Spicer, W. E.; Chye, P. W.; Garner, C. M.; Lindau, I.; Pianetta, P. The Surface Electronic Structure of III-V Compounds and the Mechanism of Fermi Level Pinning by Oxygen (Passivation) and Metals (Schottky Barriers). *Surf. Sci.* **1979**, *86* (C), 763−788.
(40) Nishimura, T.; Kita, K.; Toriumi, A. Evidence for Strong Fermi-Level Pinning Due to Metal-Induced Gap States at Metal/Germanium Interface. *Appl. Phys. Lett.* **2007**, *91* (12), 123123.
(41) Liu, Y.; Guo, J.; Zhu, E.; Liao, L.; Lee, S.-J.; Ding, M.; Shakir, I.; Gambin, V.; Huang, Y.; Duan, X. Approaching the Schottky−Mott Limit in van Der Waals Metal−semiconductor Junctions. *Nature* **2018**, *557* (7707), 696−700.
(42) Ma, X.; Liu, Q.; Xu, D.; Zhu, Y.; Kim, S.; Cui, Y.; Zhong, L.; Liu, M. Capillary-Force-Assisted Clean-Stamp Transfer of Two-Dimensional Materials. *Nano Lett.* **2017**, *17* (11), 6961−6967.
(43) Luo, Z.; Liu, H.; Spann, B. T.; Feng, Y.; Ye, P.; Chen, Y. P.; Xu, X. Measurement of In-Plane Thermal Conductivity of Ultrathin Films Using Micro-Raman Spectroscopy. *Nanoscale Microscale Thermophys. Eng.* **2014**, *18* (2), 183−193.
(44) Luo, Z.; Tian, J.; Huang, S.; Srinivasan, M.; Maassen, J.; Chen, Y. P.; Xu, X. Large Enhancement of Thermal Conductivity and Lorenz Number in Topological Insulator Thin Films. *ACS Nano* **2018**, *12* (2), 1120−1127.

DOI: 10.1021/acs.nanolett.8b05144
Nano Lett. 2019, 19, 1955−1962